

<https://doi.org/10.1038/s41612-024-00650-0>

Siberian vegetation growth intensifies monsoon precipitation in southern East Asia in late spring and early summer

Check for updates

Sang-Wook Yeh¹ ✉, Byung-Ju Sohn^{2,9} ✉, Sae-Yoon Oh¹, Se-Yong Song³, Jee-Hoon Jeong⁴, Bin Wang^{5,6}, Renguang Wu^{7,8} & Young-Min Yang⁵

Regional hydrological cycle responding to rising temperatures can have significant influences on society and human activities. We suggest a new perspective on East Asia's enhanced precipitation amount that emphasizes the role of Siberian surface warming. Increased vegetation greenness in late spring and early summer in eastern Siberia, which may be a response to global warming, acts to warm the surface by reducing the surface albedo with an increase in net absorbed shortwave radiation. Subsequently, eastern Siberia warming leads to the strengthening of anti-cyclonic atmospheric circulation over inner East Asia as well as the subtropical western North Pacific high via thermal forcing and the enhanced land-sea thermal contrast, respectively. Consequently, the anticyclonic circulation over inner East Asia transports much drier and cooler air to southern East Asia. This leads to favorable conditions for increased precipitation in combination with an increased tropical moisture flux from the subtropical western North Pacific high. Therefore, continuous Siberian vegetation growth has a potential influence on the future precipitation amount in the subtropics through vegetation–atmosphere coupled processes.

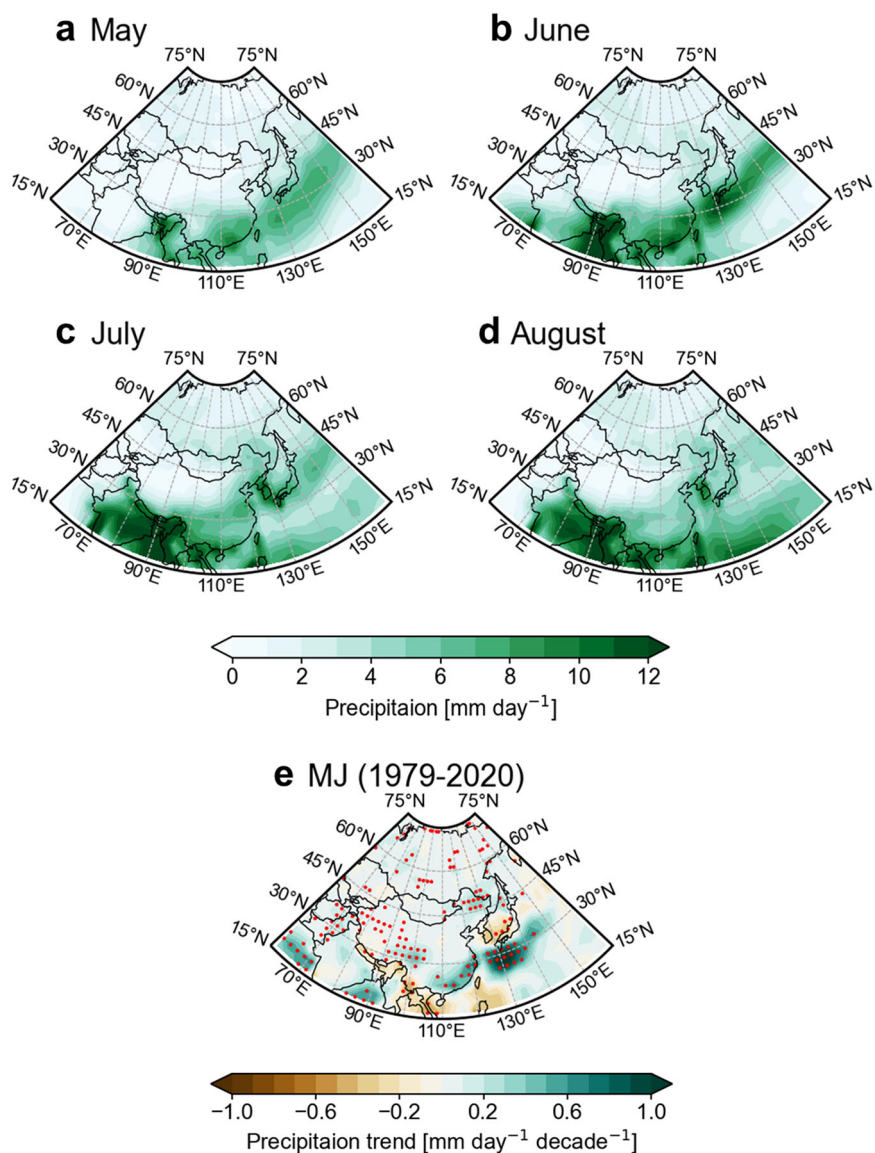
Earth's surface temperature has been steadily increasing since the industrial revolution^{1–3}. This is mostly due to anthropogenic forcing including greenhouse gas concentration increases^{4–6}. Earth's rising surface temperature directly causes changes in regional and global mean hydrological cycles^{7–9}. Hydrological cycle in the Earth system is not only a manifestation of the weather and climate but also a driving force for changes of the climate^{10,11}. However, the uncertainties exist in assessing the effects of global warming to the climate systems are due primarily to an inadequate understanding of the hydrological cycle¹⁰. For example, while increasing atmospheric moisture content is expected to intensify precipitation extremes under global warming^{12–15}, the sensitivity of precipitation to temperature is complicated and the underlying physical mechanisms related to thermodynamic and dynamical components remain unclear¹⁶.

Recently, much attention has been paid in the climate community to how the regional hydrological cycle responds to increases in the Earth's surface temperature has been given in the climate community^{17,18}. In particular, summer rainfall in East Asia is directly linked to water for agriculture, industry and life, and to an increasing trend in the frequency of extreme precipitation along the Meiyu-Baiu-Changma front^{19–23}. This requires a detailed understanding of changes in the hydrological cycle in East Asia.

The surface warming rate does have regional variations in properties including its trend, and, therefore, it is essential to understand how the regional surface warming remotely influences the trend of precipitation amount in faraway regions with other controlling factors. Among them, there are several mechanisms explaining an upward precipitation trend in

¹Department of Marine Science and Convergent Engineering, Hanyang University, Ansan, South Korea. ²School of Earth and Environmental Science, Seoul National University, Seoul, South Korea. ³Earth Research Institute, University of California, Santa Barbara, Santa Barbara, CA, USA. ⁴Department of Oceanography, Chonnam National University, Gwangju, South Korea. ⁵Key Laboratory of Meteorological Disaster, Ministry of Education (KLME)/Joint International Research Laboratory of Climate and Environment Change (ILCEC)/Collaborative Innovation Center on Forecast and Evaluation of Meteorological Disasters (CIC-FEMD), Nanjing University of Information Science and Technology, 210044 Nanjing, China. ⁶Department of Atmospheric Sciences and International Pacific Research Center, University of Hawaii, Honolulu, HI 96822, USA. ⁷School of Earth Sciences, Zhejiang University, Hangzhou, and Center for Monsoon System Research, and State Key Laboratory of Numerical Modeling for Atmospheric Sciences and Geophysical Fluid Dynamics, Institute of Atmospheric Physics, Chinese Academy of Sciences, Beijing, China. ⁸School of Earth Sciences, Zhejiang University, Hangzhou, China. ⁹School of Atmospheric Physics, Nanjing University of Information Science and Technology, Nanjing, China. ✉e-mail: swyeh@hanyang.ac.kr; sohn@snu.ac.kr

Fig. 1 | Precipitation climatology and linear trends. Climatological (1981–2010) precipitation pattern during (a) May, (b) June, (c) July, and (d) August. 1979–2020 precipitation linear trends during e May–June (MJ). Stippling shows statistically significant areas at the 95% confidence level according to a Student’s *t*-test.



southern East Asia^{24–27}. While some studies emphasize anthropogenic aerosols’ role in increased summer precipitation^{28,29}, other studies suggest that natural climate variability including El Niño and Southern Oscillation, the Indian Ocean Dipole, the Pacific Decadal Oscillation, and the Atlantic Multi-decadal Oscillation contribute to an increased occurrence of severe floods and increasing precipitation^{27,30–33}. However, there is less study of how the surface warming in the Northern Hemisphere (NH) high latitudes, where a warming trend is high^{34,35}, remotely influences East Asian monsoon precipitation. In particular, it has been reported that a large change of land cover including vegetation activity is occurring in the NH high latitudes^{36–38} and a great deal of work has been devoted to regional climate responses to the land cover change during recent decades^{39,40}.

Land cover change impacts the climate via two different processes. Biogeochemical effects modify the net fluxes of greenhouse gases, for example, CO₂, from the variations in soil carbon and vegetation^{41,42}. Biogeophysical effects can trigger the changes in the surface energy budget, which are mediated by albedo and evapotranspiration^{43,44}. Here, we suggest a biogeophysical perspective that emphasizes Siberian coupled vegetation–atmospheric processes’ influence on increased precipitation amount in southern East Asia in late spring and mid-summer.

The increase in vegetation is most evident in the Eurasian boreal forests including Siberia, which greatly accelerates the warming mainly in those regions^{45,46}. Here, through reanalysis, observational data analysis and model

experiments, we found that the increased vegetation growth in eastern Siberia in late spring and early summer has remote effects on subtropical precipitation in southern East Asia via changing the atmospheric circulations.

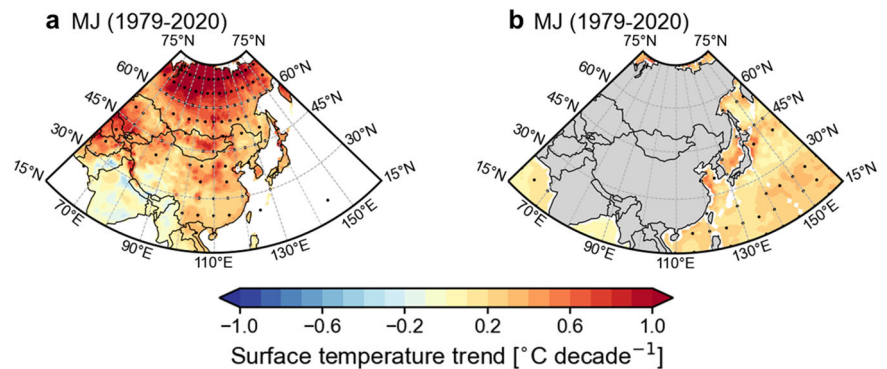
Results

An upward precipitation trend in East Asia

Northeast Asia including China, Japan, and Korea is largely influenced by Asian-Pacific monsoons consisting of the western North Pacific summer monsoon and East Asian summer monsoon between the Asian continent and the western tropical Pacific ocean⁴⁷. Climatological (1981–2010) precipitation bands extend from South Asia to the northwest Pacific in May (Fig. 1a) when the East Asian summer monsoon begins, and they become much stronger in June and July (Fig. 1b, c), when the spatial structure of the precipitation band tilts from southwest to northeast Asia. From June to July (Fig. 1b, c), the precipitation band moves to the north and its center of maximum precipitation is located over the Korean peninsula and southern Japan. In August (Fig. 1d), such a tilted structure disappears and the amount of precipitation over East Asia is reduced in East Asia compared to that in July.

This implies that there exist distinct differences of climatological (1981–2010) precipitation bands during the early and late period of the East Asian summer monsoon⁴⁸ (Supplementary Fig. 1). The purpose of this study is to

Fig. 2 | Surface temperature linear trends. 1979–2020 surface temperature linear trends over continent (a) and over the ocean (b) during MJ. Stippling shows statistically significant areas at the 95% confidence level according to a Student's *t* test.



investigate the role of Siberian surface warming, which is mainly due to increased vegetation greenness in late spring and the early summer (May to June, hereafter, MJ), on the East Asian monsoon. We mainly examined the mean structures of the early period (MJ) of the East Asian summer monsoon. Figure 1e displays the linear trend of precipitation anomalies from 1979 to 2020. During MJ, an upward precipitation trend is evident in southern East Asia including southern and eastern China in the 20°–35°N latitudinal regions (Fig. 1e). The maximum of the upward trend in precipitation in southern East Asia lies within the climatological precipitation band (Fig. 1a, b), implying that the regional hydrological cycle in East Asia during the late spring and early summer has been enhanced in recent decades.

Warming in Siberia due to vegetation climate feedback processes

We propose that vegetation climate feedback processes in the NH high latitudes such as Siberia appear to contribute to the upward precipitation trend in the southern part of East Asia (Fig. 1 and see also Supplementary Fig. 2) via changing atmospheric circulation.

Figure 2a displays the Asian continent's surface temperature trends during MJ for 1979–2020. The most striking feature is a significant surface temperature warming trend in central-to-northern Siberia north of 55°N during MJ (Fig. 2a). Indeed, NH high latitudes north of 55°N have experienced substantial continental warming in late spring and mid-summer in recent decades^{35,49,50}, with a much higher degree and faster rate than the global averages³⁵. Consequently, the land-sea thermal contrast around East Asia is also strengthened for 1979–2020 (Fig. 2a, b).

While there are several explanations about the NH high latitude surface warming^{35,49–51}, one of the most compelling is associated with vegetation-albedo feedback effects in response to global warming^{49,50}. Human-induced greenhouse gas increases and associated climate change conditions are favorable for some plant species in the NH's high latitudes and sub-Arctic regions. Over the last several decades, this phenomenon has led to increased vegetation greenness in the sub-Arctic regions like Siberia and has stimulated the expansion of shrub plants in Pan-Arctic regions^{52–55}.

The climatological (1982–2010) Normalized Difference Vegetation Index (NDVI)⁵⁶ (see Methods) are lower than 0.4–0.5 in high NH latitudes during MJ (Fig. 3a) because low temperatures and low solar radiation are primary limiting factors for vegetation's survival and growth^{57,58}. However, more vegetation and enhanced greenness during the late spring and early summer for 1982–2020 is significant (Fig. 3b), which could be due to a significant surface temperature warming trend in high NH latitudes (Fig. 2a). Enhanced high latitude vegetation greenness in response to global warming has a net positive feedback effect on surface warming, primarily by reducing surface albedo as vegetation colonizes previously snow-covered or barren surfaces^{59–61}. An increase in vegetation greenness may, in turn, increase temperature by regulating surface energy fluxes such as a net absorbed shortwave radiation. Figure 3c display linear trends in a net absorbed shortwave radiation during MJ for 1979–2020. The spatial patterns north of 55°N show a net absorbed solar radiation increase similar to surface

warming (Fig. 2a) and NDVI (Fig. 3b), implying that surface warming in the NH high latitude is mainly due to increasing net absorbed solar radiation caused by a decreasing albedo associated with an increasing vegetation greenness, i.e., vegetation-albedo feedback (Supplementary Fig. 3a). It is noteworthy that the snow cover is also significantly reduced in NH high latitudes (Supplementary Fig. 3b), where a surface warming is dominant (Fig. 2a). These results indicate that the increase of net absorbed solar radiation in NH high latitudes (Fig. 3c) could be largely explained by the albedo reduction due to either the increased vegetation greenness or the reduced snow cover.

On the other hand, biogeophysical effect is able to induce the changes in surface energy budget via evapotranspiration^{44,62}. We further calculate the linear trends in evapotranspiration during MJ for 1979–2020 and found that an increase of evapotranspiration is evident in Siberia (Fig. 3d), which is associated with an increase in vegetation greenness^{63,64}. The increase of evapotranspiration acts to cool down surface temperature, which is in contrast to surface warming in Siberia (Fig. 2a). Therefore, we conclude that an increase of net absorbed solar radiation due to either the increase of vegetation greenness or the reduced snow cover overwhelms the role of evapotranspiration on the Siberian surface temperature change, resulting in surface warming. However, significant warming over inner East Asia, including northern China and Mongolia during MJ (Fig. 2a), does not match exactly with vegetation greenness changes (Fig. 3b) or the associated net absorbed shortwave radiation feedback for the same period (Fig. 3c). This is partly because temperature is not a critical limiting factor for vegetation growth in this semi-arid region. Since this region has a large drying trend in the recent past⁶⁵, furthermore, a surface warming can be associated with a soil moisture-temperature feedback⁶⁶. Indeed, both evapotranspiration and soil moisture are reduced in inner East Asia during MJ (Fig. 3d, e). Reduced soil moisture makes it more difficult for plants to uptake soil moisture⁶⁷. This leads to the reduced evapotranspiration to the atmosphere, which reduces the latent heat flux that warms the surface temperature. Soil moisture therefore links surface temperature and latent heat flux through a feedback process. A decrease in soil moisture can reduce evaporation from land areas, which can explain a significant increase in the surface temperature in inner East Asia. Therefore, a significant warming over inner East Asia during MJ can be partly attributed to land-atmosphere coupled processes.

Siberian surface warming effects on increasing trend of precipitation amount in southern East Asia

We hypothesize that the surface warming due to the increased Siberian greenness induces changes in atmospheric circulation in the NH mid-latitudes, and may subsequently lead to precipitation increases in southern East Asia by altering regional-scale background atmospheric conditions. These changes in atmospheric circulation act to easily confine the water vapor, transported from the tropics during the late spring and early summer, in the East Asian monsoon precipitation band zone, increasing subtropical precipitation amount. The climatological structure of geopotential height (GPH) at 850 hPa during MJ is characterized by a strong pressure contrast between

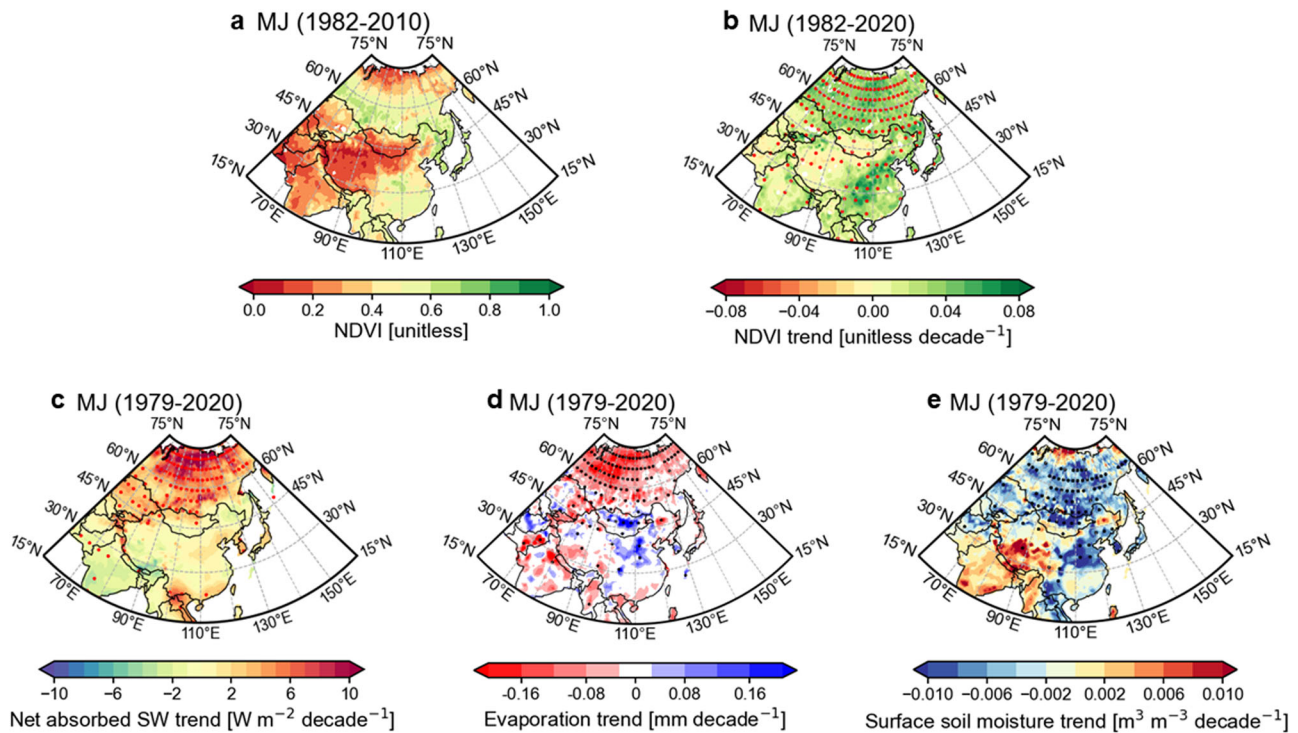


Fig. 3 | Normalized Difference Vegetation Index and trends of biogeophysical variables. **a** Climatological (1982–2010) Normalized Difference Vegetation Index (NDVI) during MJ **(b)**. NDVI linear trend during MJ for 1982–2020. **c–e** A net

absorbed shortwave radiation, evapotranspiration and surface soil moisture trends during MJ for 1979–2020, respectively. Stippling in **(b–e)** shows statistically significant areas at the 95% confidence level according to a Student’s *t* test.

land and ocean, where atmospheric pressure in the high NH latitudes is low over land, and the atmospheric pressure in the western North Pacific Ocean is high (Fig. 4a). This is largely due to the thermal contrast between land and ocean; fast warming over land induces a low-pressure system compared to the ocean⁴⁷. A center of a significant upward trend in the 850 hPa GPH during MJ (Fig. 4b, c) is slightly shifted eastward from the region where the largest warming is observed in Siberia (see Fig. 2a). This can be explained by the thermal forcing due to surface warming, which raises the lower tropospheric GPH at mid to high latitudes⁶⁸. Due to the enhanced land-sea thermal contrast, the subtropical western North Pacific High is also strengthened in June (Fig. 4c), resulting in the strengthening of southwesterlies from the subtropics into East Asia (Fig. 4c).

We suspect that the significant upward 850hPa GPH trend changes the atmospheric flow, which contributes to an enhanced low latitude vertical moisture flux convergence. Figure 5a, b analyzes the integrated moisture flux’s linear trends in the lower troposphere and convergence during May and June for 1979–2020, respectively. Fig. 5c displays the climatological (1981–2020) vertically moisture flux and its convergence. Consistent with increasing southeastern Asian precipitation during MJ (Fig. 1e), the integrated moisture flux convergence also increases in the same region in May and June. Specifically noted is the strengthening of southwesterly flux from the subtropics during June (Fig. 5b and see also Fig. 4c) is associated with the strengthening of subtropical western North Pacific high related to the enhanced land-sea thermal contrast. During July (Fig. 5c), in addition, northeasterly flux from inner East Asia is due to the strengthening of NH mid-latitude anticyclonic circulation (Fig. 4c). These fluxes lead to more favorable atmospheric conditions for moistening the southeastern Asia with tropical water vapor, resulting in an upward trend of precipitation amount in subtropical East Asia.

Idealized model experiments

To support the above hypothesis, we conducted two idealized climate model experiments in which the Simple Land Interface Model⁶⁹ is coupled to the

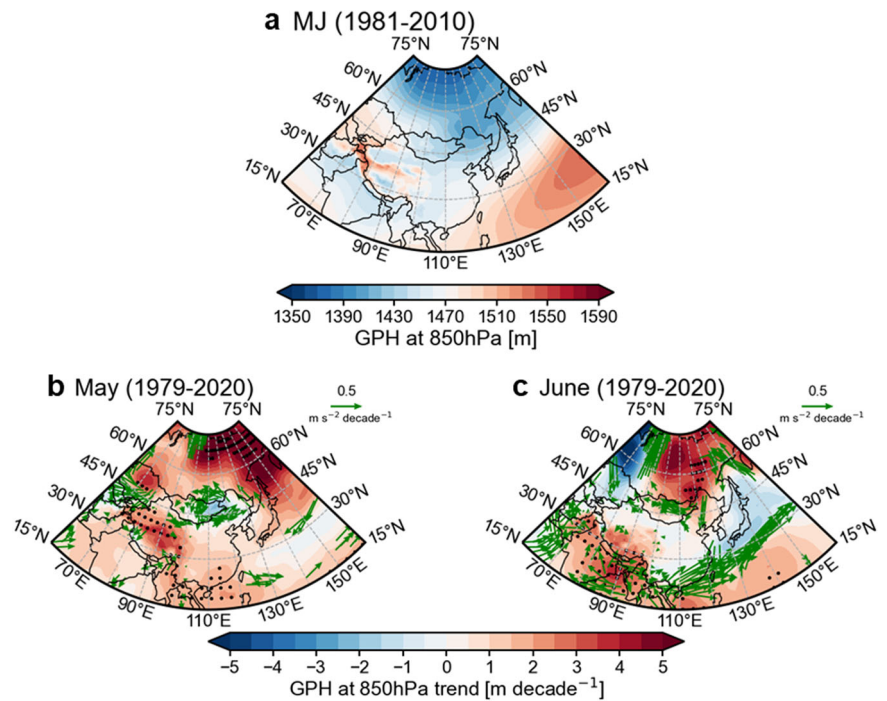
Community Atmosphere Model version 5 with an interactive slab ocean model⁷⁰ and the Los Alamos Sea Ice Model for interactive sea ice⁷¹ (Methods), to quantify how the surface albedo changes due to the increased vegetation in Siberia impact the precipitation amount in subtropical East Asia.

The first is a control run in which the climatological background land albedo obtained from ERA5 reanalysis dataset is prescribed (hereafter, referred to as CTL_Exp). The second is the idealized run in which the albedos are reduced in NH high latitudes where the albedo linear trend is statistically significantly reduced in the reanalysis dataset (Supplementary Figs. 3a, b and 4) during MJ in order to mimic the increased vegetation-albedo feedback (hereafter, Albedo_Exp) (see Methods). In NH high latitudes, among the effects of increased vegetation on the climate system, the effect of radiative change due to albedo reduction is dominant^{49,50}. Therefore, this experimental design is an appropriate assumption to simulate the effect of reduced albedo due to the increased vegetation.

Due to the imposed albedo changes, the total albedo in the Albedo_Exp is reduced over the central-to-northern Siberia region (Supplementary Figs. 5a, b). The albedo averaged in the central-to-northern Siberia region (60°–160°E, 55°–75°N) between two experiments (Albedo_Exp minus CTL_Exp) is -0.023 during MJ. Note that the albedo difference in the same regions between two periods (2011–2020 minus 1979–1988) is -0.07 during MJ in the reanalysis dataset (Supplementary Fig. 3). Therefore, the Albedo_Exp may explain about 32% of albedo changes during MJ in the reanalysis dataset for 1979–2020. We further analyze the albedo product from the Satellite Application Facility on Climate Monitoring’s cloud, albedo, and surface radiation dataset from advanced very high-resolution radiometer data, CLARA-A3⁷² for the period of 1979–2020 (Supplementary Fig. 5c and Methods). The albedo difference over the central to northern Siberia region between two periods (2011–2020 minus 1979–1988) is -0.03 during MJ, which is similar to that in the model experiment.

Figure 6 displays the differences in surface temperature, GPH at 850hPa, vertically integrated moisture flux, and precipitation between the

Fig. 4 | Climatological geopotential height at 850hPa and its linear trends with 850hPa horizontal winds. **a** Climatological (1981–2010) structure of 850hPa geopotential height during a MJ. **b, c** 1979–2020 geopotential height and horizontal winds linear trends during May and June. Stippling in **(b, c)** shows statistically significant areas at the 90% confidence level according to a Student’s *t* test. Linear trends of 850 hPa horizontal winds above the 90% confidence level are displayed only in **(b, c)**.



Albedo_Exp and CTL_Exp during MJ. There are some discrepancies in the spatial structures compared with the reanalysis dataset because the model difference represents the influence of the reduced land surface albedo in NH high latitudes only. In spite of this, the surface temperature increases in Siberia during MJ (Fig. 6a) due to the increased net absorbed shortwave radiation (Supplementary Figs. 5a). The anti-cyclonic circulation is simulated in NH high latitudes during MJ although the statistical significance is very limited (Fig. 6b). On the other hand, the strengthening of subtropical western North Pacific high is very clear in the simulated results (Fig. 6b). Such phenomenon might be induced by the enhanced land-sea thermal contrast, which is mainly affected by the Siberian surface warming (Fig. 6a).

Consequently, the increased precipitation in southeastern East Asia, including southern and central China, Japan, and Korea, is simulated along with the enhanced moisture convergence during MJ (Fig. 6c, d) although the simulated precipitation response shifted northward compared with observation. The precipitation averaged in the southeastern Asia (105°–140°E, 22°–36°N) between two experiments is 0.51 mm/day during MJ, and the amount of precipitation increased from 1979–988 to 2011–2020 is 1.09 mm/day during MJ in the observation (Fig. 1e). Therefore, the Albedo_Exp explains about 47% of observed precipitation changes during MJ for 1979–2020. These results support our hypothesis that the climate effects of increased vegetation growth in Siberia play an important role in precipitation increases in southeastern Asia during the late spring and early summer through the regional atmospheric circulation change.

Conclusion and discussion

By analyzing observational and reanalysis datasets along with idealized numerical experiments, we suggest a biogeophysical effect from vegetation–atmosphere coupled processes in Siberia, which, by way of altering atmospheric circulation, increases late spring and early summer precipitation in the subtropical Asia. While vegetation–albedo feedback processes may largely contribute to Siberia’s warming^{35,49,50}, we emphasize that such influence is not limited regionally and can reach the subtropics. The Siberia surface warming is associated with the strengthening of anticyclonic circulations in inner East Asia as well as the subtropical western North

Pacific high, which changes the structure of the vertically integrated moisture flux and its convergence/divergence in the subtropics. This leads to the increased precipitation in the southeastern Asia. Therefore, vegetation greenness over Siberia, which could be associated with global warming^{73,74}, influences changes in the subtropical hydrological cycle. This implies that a rapid change of vegetation activity in NH high latitudes should be carefully considered to understand the changes in the hydrological cycle in low latitude regions in future climate. However, it is necessary to quantify how much the surface warming and albedo changes due to the increased vegetation growth drives the atmospheric circulation changes compared to the roles of either non-albedo driven surface warming or non-vegetation driven albedo change, which is not precisely examined in the present study.

Methods

Dataset

We obtained monthly observational precipitation fields for 1979–2020 from the Global Precipitation Climatology Project (GPCP) version 2.3⁷⁵. The GPCP version 2.3 product provides precipitation datasets at a spatial resolution of 2.5° from the integration of station observations and satellite estimates. For 1979–2020 atmospheric fields, forecast albedo data and soil moisture, we used the monthly European Centre for Medium-Range Weather Forecasts (ECMWF) fifth major global reanalysis (ERA5)⁷⁶. To obtain the anomalies of the atmospheric fields, we used the monthly climatological period of 1981–2010 (30-years). We additionally analyzed the shortwave albedo obtained from the Satellite Application Facility on Climate Monitoring’s cloud, albedo, and surface radiation dataset from advanced very-high-resolution radiometer data, CLARA-A3 for the period of 1979–2020⁷².

Normalized Difference Vegetation Index

We used Normalized Difference Vegetation Index (NDVI) datasets from the AVHRR sensor, which quantifies vegetation by evaluating the difference between near-infrared and red light⁷⁷. Monthly NDVI data from 1982 to 2020 was obtained using the Maximum Value Composite (MVC) method^{78,79}, where the highest value is selected

Fig. 5 | Vertically integrated moisture flux and its convergence linear trends. **a, b** 1979–2020 vertically integrated moisture flux (vector) and its convergence (shading) linear trends during May and June, respectively. Shading in **(a, b)** represents convergence (red) and divergence (blue) of the vertically integrated moisture flux. Stippling shows statistically significant areas for the vertically integrated moisture flux convergence at the 90% confidence level according to a Student’s *t* test. **c** Climatological (1981–2010) vertically integrated moisture flux and convergence/divergence during MJ. Arrows represent the vertically integrated moisture flux vector. Scale in **(a–c)** is shown in the upper right above figure. Shading represents convergence (red) and divergence (blue) of the vertically integrated moisture flux.

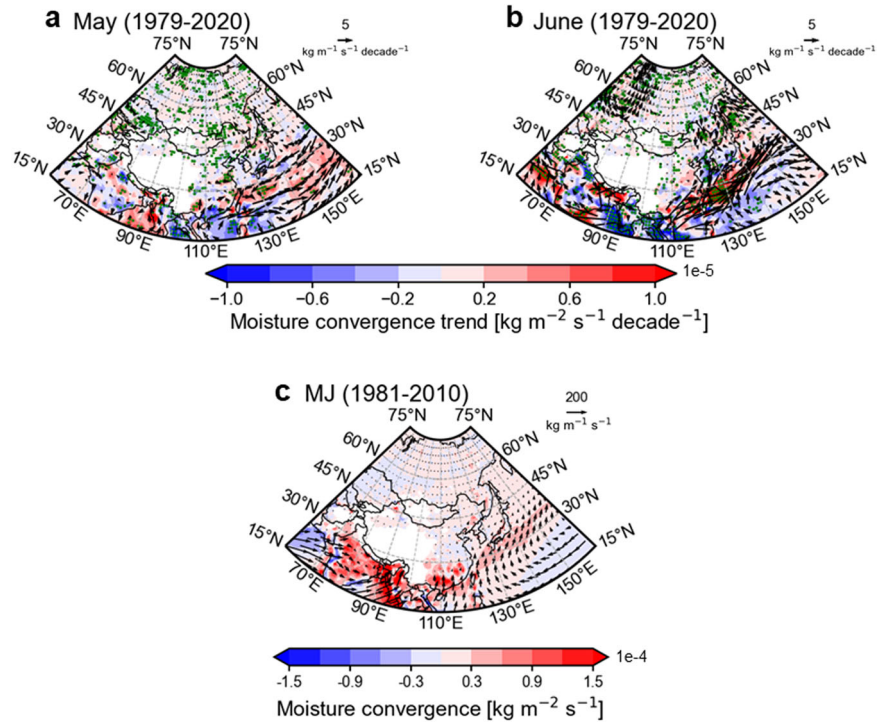
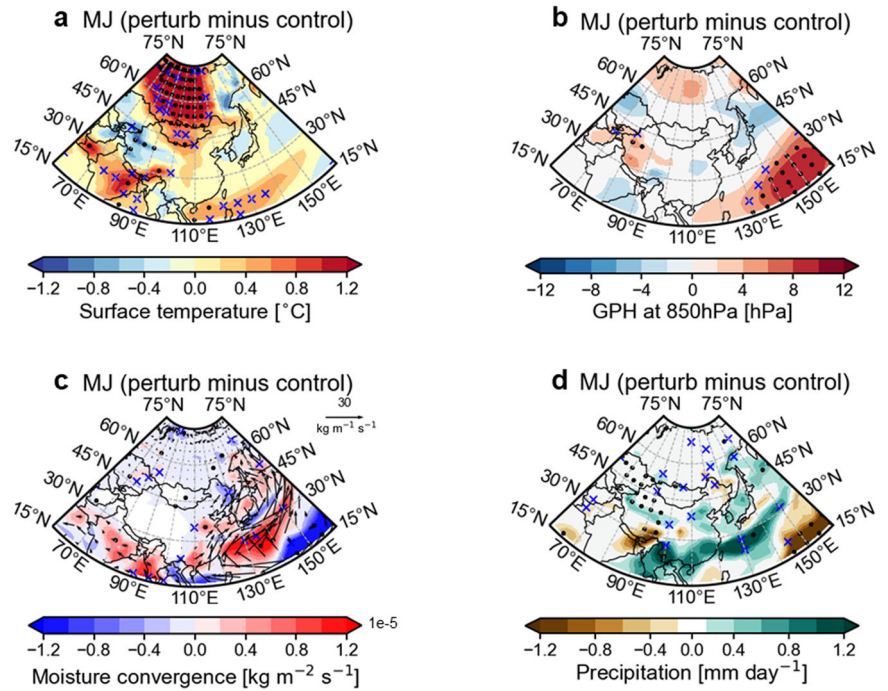


Fig. 6 | Model responses for the reduced land surface albedo in Siberia. **a** Changes in surface temperature for the reduced land surface albedo in Siberia during MJ. **b–d** as in **(a)** but for the 850 hPa geopotential height, vertically integrated moisture flux and precipitation, respectively. Stippling and blue crosses show statistically significant areas at the 95% and 90% confidence level according to a Student’s *t* test, respectively.



from each NDVI value for each grid. MVC methods can minimize common problems in single-date remote sensing studies such as cloud contamination, atmospheric attenuation, and surface directional reflection. Note that we obtained the NDVI anomalies for 1982–2010 monthly climatology.

Vertically integrated moisture flux

The vertically integrated moisture flux ($\text{kg m}^{-2} \text{s}^{-1}$) was calculated by integrating specific humidity (q) (g kg^{-1}) and horizontal wind vector (\mathbf{V}) (m s^{-1}) values from the surface pressure to the lower

tropospheric layer (850 hPa) as follows:

$$\text{VIMF} = \frac{1}{g} \int_{850\text{hPa}}^{p_s} (q\mathbf{V}) dp \tag{1}$$

where g (m s^{-2}) is the gravitational acceleration and p_s (N m^{-2}) is the surface pressure. Because the atmospheric water vapor transport is most evident in the lower troposphere, we integrated vertically from the surface pressure to 850hPa. The monthly vertically integrated moisture flux is obtained by using the daily specific humidity and horizontal winds in relation to

transient eddies on daily time scales and then we averaged in May–June and June–July, respectively.

Pattern correlation

To quantify the resemblance among the climatological mean and trend fields, we computed the area-weighted pattern correlation (AWPC) as follows⁸⁰:

$$\text{AWPC} = \frac{\sum_{i=1}^n \sum_{j=1}^m W_{ij} X_{ij} Y_{ij}}{\left(\sum_{i=1}^n \sum_{j=1}^m W_{ij} X_{ij}^2 \right)^{\frac{1}{2}} \left(\sum_{i=1}^n \sum_{j=1}^m W_{ij} Y_{ij}^2 \right)^{\frac{1}{2}}} \quad (2)$$

where W_{ij} is an area-weight coefficient and ij is the latitude/longitude index of the spatial pattern X and Y consisting of n and m grid points in Eq. (2).

Statistical significant test

We used a Student's t -test to obtain the statistical significance in the trend fields. t -test is a statistical hypothesis test in which the test statistic follows a Student's t distribution under the null hypothesis. A t -test is two-sided (also termed two-tailed), specifying whether the observed trend is larger or smaller than the hypothesized mean. The test statistic t in Eq.(3) is then calculated as follows

$$t = \frac{b - \beta_1}{S_b} \quad (3)$$

(b : sample slope, β_1 : (null) hypothesized slope, S_b : standard error of the slope)

If the t -statistic is more extreme than the critical value determined by the appropriate reference distribution, the null hypothesis is rejected. The critical value depends on the significance level of the test (the probability of erroneously rejecting the null hypothesis). Note that we also used a different statistical test, i.e., Mann–Kendall test⁸¹ to obtain the statistical robustness and reached to the similar results.

Idealized model experiments

To quantify the impact of vegetation–atmosphere coupling on the regional hydrological cycle, we conducted idealized climate model experiments. The model used in this study is the SLIM⁶⁹ which couples to the CESM⁸² in place of the CLM5⁸³. The SLIM allows us to perturb a single surface property while holding the rest of the land surface properties fixed. As such, this idealized approach to land surface modeling has been utilized to quantify how changes in specific aspects of the land surface impact atmospheric circulation and surface climate response^{69,84,85}. The SLIM is coupled to the CAM5 with an interactive SOM⁷⁰ and the CICE5⁷¹. These coupled simulations allow for atmospheric feedbacks related to the land–atmosphere coupling that plays a vital role in defining temperature responses to albedo changes over the mid-to-high latitudes⁶⁹. The SOM configuration also enables atmospheric signals to propagate farther than a fixed surface boundary condition, which is important for allowing shifts in large-scale atmospheric circulation and precipitation response driven by changes in land surface properties^{86–88}. Thus, this idealized modeling framework is a suitable tool for understanding atmospheric responses to changes in land surface properties due to vegetation–atmosphere coupling processes.

We designed our two experiments by modifying the snow-free land albedo over non-glaciated regions as follows: We specified albedo values for four solar radiation streams, direct visible, direct near-infrared, diffuse visible, and diffuse near-infrared light. The control experiment (CTL_Exp) was prescribed with monthly climatological background land albedo for these four radiation streams from ERA5 reanalysis dataset⁷⁶. In the albedo perturbation experiment (Albedo_Exp), we imposed decreases in land albedo for direct and diffuse visible shortwave radiation spectra only, which is directly involved in the vegetation albedo processes⁸⁹, over NH high latitudes where the albedo linear trend is statistically significantly reduced during May-to-June in the reanalysis dataset (Supplementary Figs. 3, 5). We conducted the

Albedo_Exp in which the albedo for direct and diffuse visible shortwave radiation has been decreased by multiplying it by 0.5. The CTL_Exp and Albedo_Exp were integrated for 50 years with a fixed CO₂ concentration of 367 ppm. We discarded output data from the first 30 years as spin-up and used the last 20 years for analysis in which the atmospheric variables simulated in experiments are stabilized in terms of global mean surface temperature (Supplementary Fig. 6). It should be noted that the results when we used the last 40, 30, and 10 years for analysis are almost identical.

Data availability

The GPCP precipitation data are acquired from <https://psl.noaa.gov/data/gridded/data.gpcp.html>. ERA5 reanalysis data are acquired from <https://cds.climate.copernicus.eu/#/home>. The AVHRR NDVI data are acquired from <https://climatedataguide.ucar.edu/climate-data/ndvi-normalized-difference-vegetation-index-noaa-avhrr>. The CLARA-A3 dataset is obtained from <https://www.cmsaf.eu/>. The code of CESM is available from <http://www.cesm.ucar.edu/models> (CESM code website). The SLIM source code is hosted on the ESCOMP repository: <https://github.com/ESCOMP/SimpleLand>. All coding used to generate this study's results is available on request from the authors.

Code availability

The python code used to produce the figures of this study is available upon request from the authors (sysong619@gmail.com or dhto977@gmail.com).

Received: 12 November 2023; Accepted: 15 April 2024;

Published online: 02 May 2024

References

- Hansen, J. et al. Earth's energy imbalance: confirmation and implications. *Science* **308**, 1431–1435 (2005).
- IPCC *Climate Change 2001: The Scientific Basis* (Cambridge Univ. Press, 2001).
- Karl, T. R. & Trenberth, K. E. Modern global climate change. *Science* **302**, 1719–1723 (2003).
- Manabe, S. & Wetherald, R. T. The effects of doubling the CO₂ concentration on the climate of a general circulation model. *J. Atmos. Sci.* **32**, 3–15 (1975).
- Hansen, J. et al. Climate impact of increasing atmospheric carbon dioxide. *Science* **213**, 957–966 (1981).
- Wang, W., Yung, Y., Lacic, A., Mo, T. & Hansen, J. Greenhouse effects due to man-made perturbations of trace gases. *Science* **194**, 685–690 (1976).
- Alexander, L. V. et al. Global observed changes in daily climate extremes of temperature and precipitation. *J. Geophys. Res. Atmos.* **111** (2006).
- Allan, R. P. & Soden, B. J. Atmospheric warming and the amplification of precipitation extremes. *Science* **321**, 1481–1484 (2008).
- Trenberth, K. E., Dai, A., Rasmussen, R. M. & Parsons, D. B. The changing character of precipitation. *Bull. Am. Meteorol. Soc.* **84**, 1205–1218 (2003).
- Chahine, M. T. The hydrological cycle and its influence on climate. *Nature* **359**, 373–380 (1992).
- Williams, P. D., Guilyardi, E., Sutton, R., Gregory, J. & Madec, G. A new feedback on climate change from the hydrological cycle. *Geophys. Res. Lett.* **34** (2007).
- Papalexiou, S. M. & Montanari, A. Global and regional increase of precipitation extremes under global warming. *Water Resour. Res.* **55**, 4901–4914 (2019).
- Sohn, B.-J., Yeh, S.-W., Lee, A. & Lau, W. K. Regulation of atmospheric circulation controlling the tropical Pacific precipitation change in response to CO₂ increases. *Nat. Commun.* **10**, 1108 (2019).
- Zhang, W., Zhou, T., Zou, L., Zhang, L. & Chen, X. Reduced exposure to extreme precipitation from 0.5 C less warming in global land monsoon regions. *Nat. Commun.* **9**, 3153 (2018).

15. Chen, Z. et al. Global land monsoon precipitation changes in CMIP6 projections. *Geophys. Res. Lett.* **47**, e2019GL086902 (2020).
16. Gu, L. et al. Large anomalies in future extreme precipitation sensitivity driven by atmospheric dynamics. *Nat. Commun.* **14**, 3197 (2023).
17. Liu, L., Gao, J. & Wu, S. Warming of 0.5 °C may cause double the economic loss and increase the population affected by floods in China. *Nat. Hazards Earth Syst. Sci.* **22**, 1577–1590 (2022).
18. Mirza, M. M. Q. Climate change, flooding in South Asia and implications. *Reg. Environ. Change* **11**, 95–107 (2011).
19. Moon, S. et al. Anthropogenic warming induced intensification of summer monsoon frontal precipitation over East Asia. *Sci. Adv.* **9**, eadh4195 (2023).
20. Min, S.-K. et al. Human contribution to the 2020 summer successive hot-wet extremes in South Korea. *Bull. Am. Meteorol. Soc.* **103**, S90–S97 (2022).
21. Zeng, W., Chen, G., Bai, L., Liu, Q. & Wen, Z. Multiscale processes of heavy rainfall over East Asia in summer 2020: Diurnal cycle in response to synoptic disturbances. *Mon. Weather Rev.* **150**, 1355–1376 (2022).
22. Wang, S. S.-Y. et al. Consecutive extreme flooding and heat wave in Japan: Are they becoming a norm? *Atmos. Sci. Lett.* **20**, e993 (2019).
23. Takahashi, H. G. & Fujinami, H. Recent decadal enhancement of Meiyu–Baiu heavy rainfall over East Asia. *Sci. Rep.* **11**, 13665 (2021).
24. Chen, Y. & Zhai, P. Synoptic-scale precursors of the East Asia/Pacific teleconnection pattern responsible for persistent extreme precipitation in the Yangtze River Valley. *Q. J. R. Meteorol. Soc.* **141**, 1389–1403 (2015).
25. Guan, Y., Zheng, F., Zhang, X. & Wang, B. Trends and variability of daily precipitation and extremes during 1960–2012 in the Yangtze River Basin, China. *Int. J. Climatol.* **37**, 1282–1298 (2017).
26. Zhang, Q. et al. Spatial and temporal variability of precipitation maxima during 1960–2005 in the Yangtze River basin and possible association with large-scale circulation. *J. Hydrol.* **353**, 215–227 (2008).
27. Yang, F. & Lau, K. M. Trend and variability of China precipitation in spring and summer: linkage to sea-surface temperatures. *Int. J. Climatol.: J. R. Meteorol. Soc.* **24**, 1625–1644 (2004).
28. Menon, S., Hansen, J., Nazarenko, L. & Luo, Y. Climate effects of black carbon aerosols in China and India. *Science* **297**, 2250–2253 (2002).
29. Xu, Q. Abrupt change of the mid-summer climate in central east China by the influence of atmospheric pollution. *Atmos. Environ.* **35**, 5029–5040 (2001).
30. Xiao, M., Zhang, Q. & Singh, V. P. Influences of ENSO, NAO, IOD and PDO on seasonal precipitation regimes in the Yangtze River basin, China. *Int. J. Climatol.* **35**, 3556–3567 (2015).
31. Cao, F. et al. Contributions of natural climate variability on the trends of seasonal precipitation extremes over China. *Int. J. Climatol.* **41**, 5226–5242 (2021).
32. Li, X. et al. Changes in precipitation extremes in the Yangtze River Basin during 1960–2019 and the association with global warming, ENSO, and local effects. *Sci. Total Environ.* **760**, 144244 (2021).
33. Lu, R., Dong, B. & Ding, H. Impact of the Atlantic Multidecadal Oscillation on the Asian summer monsoon. *Geophys. Res. Lett.* **33** (2006).
34. Comiso, J. C. & Hall, D. K. Climate trends in the Arctic as observed from space. *WIREs Clim. Change* **5**, 389–409 (2014).
35. Serreze, M. et al. Observational evidence of recent change in the northern high-latitude environment. *Clim. Change* **46**, 159–207 (2000).
36. Lambin, E. F. & Geist, H. J. *Land-Use and Land-Cover Change: Local Processes and Global Impacts* (Springer Science & Business Media, 2008).
37. Tchepakova, N. M., Parfenova, E. & Soja, A. The effects of climate, permafrost and fire on vegetation change in Siberia in a changing climate. *Environ. Res. Lett.* **4**, 045013 (2009).
38. Xia, J. et al. Terrestrial carbon cycle affected by non-uniform climate warming. *Nat. Geosci.* **7**, 173–180 (2014).
39. Devaraju, N., de Noblet-Ducoudré, N., Quesada, B. & Bala, G. Quantifying the relative importance of direct and indirect biophysical effects of deforestation on surface temperature and teleconnections. *J. Clim.* **31**, 3811–3829 (2018).
40. Huang, H. et al. Assessing global and regional effects of reconstructed land-use and land-cover change on climate since 1950 using a coupled land–atmosphere–ocean model. *J. Clim.* **33**, 8997–9013 (2020).
41. Jia, G. et al. *Climate Change and Land. Chapter 2: Land-Climate Interactions* (IPCC Special Report on Global Warming, 2019).
42. Sitch, S. et al. Impacts of future land cover changes on atmospheric CO₂ and climate. *Glob. Biogeochem. Cycles* **19**, GB2013 (2005).
43. Brovkin, V., Raddatz, T., Reick, C. H., Claussen, M. & Gayler, V. Global biogeophysical interactions between forest and climate. *Geophys. Res. Lett.* **36** (2009).
44. Mahmood, R. et al. Land cover changes and their biogeophysical effects on climate. *Int. J. Climatol.* **34**, 929–953 (2014).
45. Jeong, J.-H. et al. Greening in the circumpolar high-latitude may amplify warming in the growing season. *Clim. Dyn.* **38**, 1421–1431 (2012).
46. Zhang, W. et al. Self-amplifying feedbacks accelerate greening and warming of the Arctic. *Geophys. Res. Lett.* **45**, 7102–7111 (2018).
47. Yihui, D. & Chan, J. C. The East Asian summer monsoon: an overview. *Meteorol. Atmos. Phys.* **89**, 117–142 (2005).
48. Wang, B., Liu, J., Yang, J., Zhou, T. & Wu, Z. Distinct principal modes of early and late summer rainfall anomalies in East Asia. *J. Clim.* **22**, 3864–3875 (2009).
49. Chapin, F. S. et al. Role of land-surface changes in Arctic summer warming. *Science* **310**, 657–660 (2005).
50. Swann, A. L., Fung, I. Y., Levis, S., Bonan, G. B. & Doney, S. C. Changes in Arctic vegetation amplify high-latitude warming through the greenhouse effect. *Proc. Natl Acad. Sci. USA* **107**, 1295–1300 (2010).
51. Kug, J. S., Choi, D. H., Jin, F. F., Kwon, W. T. & Ren, H. L. Role of synoptic eddy feedback on polar climate responses to the anthropogenic forcing. *Geophys. Res. Lett.* **37** (2010).
52. Jeong, S.-J., HO, C.-H., GIM, H.-J. & Brown, M. E. Phenology shifts at start vs. end of growing season in temperate vegetation over the Northern Hemisphere for the period 1982–2008. *Glob. Change Biol.* **17**, 2385–2399 (2011).
53. Tape, K., Sturm, M. & Racine, C. The evidence for shrub expansion in Northern Alaska and the Pan-Arctic. *Glob. Change Biol.* **12**, 686–702 (2006).
54. Xu, L. et al. Temperature and vegetation seasonality diminishment over northern lands. *Nat. Clim. Change* **3**, 581–586 (2013).
55. Zhou, L. et al. Variations in northern vegetation activity inferred from satellite data of vegetation index during 1981 to 1999. *J. Geophys. Res. Atmos.* **106**, 20069–20083 (2001).
56. DeFries, R. S. & Townshend, J. NDVI-derived land cover classifications at a global scale. *Int. J. Remote. Sens.* **15**, 3567–3586 (1994).
57. Chapin, F. S. Direct and indirect effects of temperature on arctic plants. *Polar. Biol.* **2**, 47–52 (1983).
58. Chapin, F. S., Bloom, A. J., Field, C. B. & Waring, R. H. Plant responses to multiple environmental factors. *Bioscience* **37**, 49–57 (1987).
59. Levis, S., Foley, J. & Pollard, D. Potential high-latitude vegetation feedbacks on CO₂-induced climate change. *Geophys. Res. Lett.* **26**, 747–750 (1999).
60. O’ishi, R. & Abe-Ouchi, A. Influence of dynamic vegetation on climate change arising from increasing CO₂. *Clim. Dyn.* **33**, 645–663 (2009).
61. Zhang, J. & Walsh, J. E. Relative impacts of vegetation coverage and leaf area index on climate change in a greener north. *Geophys. Res. Lett.* **34** (2007).

62. Betts, R. A., Falloon, P. D., Goldewijk, K. K. & Ramankutty, N. Biogeophysical effects of land use on climate: Model simulations of radiative forcing and large-scale temperature change. *Agr. For. Meteorol.* **142**, 216–233 (2007).
63. Shi, S., Wang, P. & Yu, J. Vegetation greening and climate change promote an increase in evapotranspiration across Siberia. *J. Hydrol.* **610**, 127965 (2022).
64. Zhang, K. et al. Vegetation greening and climate change promote multidecadal rises of global land evapotranspiration. *Sci. Rep.* **5**, 1–9 (2015).
65. Cheng, S., Guan, X., Huang, J., Ji, F. & Guo, R. Long-term trend and variability of soil moisture over East Asia. *J. Geophys. Res. Atmos.* **120**, 8658–8670 (2015).
66. Zhang, P. et al. Abrupt shift to hotter and drier climate over inner East Asia beyond the tipping point. *Science* **370**, 1095–1099 (2020).
67. Seneviratne, S. I. et al. Investigating soil moisture–climate interactions in a changing climate: a review. *Earth Sci. Rev.* **99**, 125–161 (2010).
68. Cohen, J. et al. Recent Arctic amplification and extreme mid-latitude weather. *Nat. Geosci.* **7**, 627–637 (2014).
69. Laguë, M. M., Bonan, G. B. & Swann, A. L. Separating the impact of individual land surface properties on the terrestrial surface energy budget in both the coupled and uncoupled land–atmosphere system. *J. Clim.* **32**, 5725–5744 (2019).
70. Neale, R. B. et al. *Description of the NCAR Community Atmosphere Model (CAM 5.0)*. NCAR Technical Note NCAR/TN-486+STR (National Center of Atmospheric Research, 2012).
71. Hunke, E. C., Lipscomb, W. H., Turner, A. K., Jeffery, N. & Elliott, S. *CICE: The Los Alamos Sea Ice Model Documentation and Software User's Manual Version 5.1* Technical Report (Los Alamos National Laboratory, 2015).
72. Karlsson, K.-G. et al. CLARA-A3: The third edition of the AVHRR-based CM SAF climate data record on clouds, radiation and surface albedo covering the period 1979 to 2023. *Earth Syst. Sci. Data* **2023**, 1–42 (2023).
73. Piao, S. et al. Characteristics, drivers and feedbacks of global greening. *Nat. Rev. Earth Environ.* **1**, 14–27 (2020).
74. Zhu, Z. et al. Greening of the Earth and its drivers. *Nat. Clim. Change* **6**, 791–795 (2016).
75. Adler, R. F. et al. The Global Precipitation Climatology Project (GPCP) monthly analysis (new version 2.3) and a review of 2017 global precipitation. *Atmosphere* **9**, 138 (2018).
76. Hersbach, H. et al. The ERA5 global reanalysis. *Q. J. R. Meteorol. Soc.* **146**, 1999–2049 (2020).
77. Vermote, E. et al. NOAA Climate Data Record (CDR) of Normalized Difference Vegetation Index (NDVI), Version 5. <https://doi.org/10.7289/V5ZG6QH9> (2018).
78. Mao, D., Wang, Z., Luo, L. & Ren, C. Integrating AVHRR and MODIS data to monitor NDVI changes and their relationships with climatic parameters in Northeast China. *Int. J. Appl. Earth Obs.* **18**, 528–536 (2012).
79. Holben, B. N. Characteristics of maximum-value composite images from temporal AVHRR data. *Int. J. Remote. Sens.* **7**, 1417–1434 (1986).
80. Huang, W., Wang, B., Wright, J. S. & Chen, R. On the non-stationary relationship between the Siberian High and Arctic Oscillation. *PLoS ONE* **11**, e0158122 (2016).
81. Mann, H. B. Nonparametric tests against trend. *Econometrica* **13**, 245–259 (1945).
82. Hurrell, J. W. et al. The community earth system model: a framework for collaborative research. *Bull. Am. Meteorol. Soc.* **94**, 1339–1360 (2013).
83. Lawrence, D. M. et al. The Community Land Model version 5: Description of new features, benchmarking, and impact of forcing uncertainty. *J. Adv. Model. Earth Syst.* **11**, 4245–4287 (2019).
84. Kim, J. E., Laguë, M. M., Pennypacker, S., Dawson, E. & Swann, A. L. Evaporative Resistance is of Equal Importance as Surface Albedo in High-Latitude Surface Temperatures Due to Cloud Feedbacks. *Geophys. Res. Lett.* **47**, e2019GL085663 (2020).
85. Laguë, M. M., Swann, A. L. & Boos, W. R. Radiative feedbacks on land surface change and associated tropical precipitation shifts. *J. Clim.*, 1–63 (2021).
86. Swann, A. L., Fung, I. Y. & Chiang, J. C. Mid-latitude afforestation shifts general circulation and tropical precipitation. *Proc. Natl Acad. Sci. USA* **109**, 712–716 (2012).
87. Davin, E. L. & de Noblet-Ducoudré, N. Climatic impact of global-scale deforestation: radiative versus nonradiative processes. *J. Clim.* **23**, 97–112 (2010).
88. Bonan, G. B., Pollard, D. & Thompson, S. L. Effects of boreal forest vegetation on global climate. *Nature* **359**, 716–718 (1992).
89. Zheng, L. et al. Spatial, temporal, and spectral variations in albedo due to vegetation changes in China's grasslands. *ISPRS J. Photogramm. Remote Sens.* **152**, 1–12 (2019).

Acknowledgements

This research was also supported by the Research Program for the carbon cycle between oceans, land, and atmosphere of the NRF funded by the Ministry of Science and ICT (2021M3I6A1086803) and also supported by the Korea Environment Industry and Technology Institute (KEITI) through Climate Change R&D Project for New Climate Regime funded by Korea Ministry of Environment (MOE) (2022003560001).

Author contributions

S.W.Y. and B.J.S. conceived of the study and S.Y.S. and S.Y.O. conducted analysis, and S.W.Y. wrote the manuscript with comments and input from B.J.S., S.Y.S., S.Y.O., J.H.J., B.W., R.W. and Y.M.Y. All authors contributed to the writing of the manuscript and the improvement of the manuscript.

Competing interests

The authors declare no competing interests.

Additional information

Supplementary information The online version contains supplementary material available at <https://doi.org/10.1038/s41612-024-00650-0>.

Correspondence and requests for materials should be addressed to Sang-Wook Yeh or Byung-Ju Sohn.

Reprints and permissions information is available at <http://www.nature.com/reprints>

Publisher's note Springer Nature remains neutral with regard to jurisdictional claims in published maps and institutional affiliations.

Open Access This article is licensed under a Creative Commons Attribution 4.0 International License, which permits use, sharing, adaptation, distribution and reproduction in any medium or format, as long as you give appropriate credit to the original author(s) and the source, provide a link to the Creative Commons licence, and indicate if changes were made. The images or other third party material in this article are included in the article's Creative Commons licence, unless indicated otherwise in a credit line to the material. If material is not included in the article's Creative Commons licence and your intended use is not permitted by statutory regulation or exceeds the permitted use, you will need to obtain permission directly from the copyright holder. To view a copy of this licence, visit <http://creativecommons.org/licenses/by/4.0/>.

© The Author(s) 2024